International Journal of Minerals, Metallurgy and Materials
Accepted manuscript, https://doi.org/10.1007/s12613-024-3027-0

Design of PbS quantum dots-$PbMoO_4$-MoS_2 ternary nanocomposites for highly selective NO_2 sensing at room temperature

Jinzhou Bai, *Yanbai Shen*✉, *Ang Li*, *Meili Wu*, *Hong Xiao*,*Qiang Zhao*, *Sikai Zhao*✉, *Wengang Liu*, *and Baoyu Cui*

School of Resources and Civil Engineering, Northeastern University, Shenyang 110819, China

✉Corresponding authors: Yanbai Shen E-mail: shenyanbai@mail.neu.edu.cn; Sikai Zhao E-mail: zhaosikai@mail.neu.edu.cn

Abstract

Traditional resistive semiconductor gas sensors suffer from high operating temperature and poor selectivity. Herein, a highly selective NO_2 sensor based on PbS quantum dots-$PbMoO_4$-MoS_2 ternary nanocomposites operating at room temperature was fabricated to address the issue. The ternary nanocomposites were synthesized via an in-situ method, yielding PbS quantum dots (QDs) with an average size of ~10 nm and $PbMoO_4$ nanoparticles in the 10-20 nm range, uniformly distributed on ultrathin MoS_2 nanosheets with an average thickness of ~7 nm. The optimized sensor demonstrated a significant improvement in response to 1 ppm NO_2 at 25°C, achieving a response of 44.5%, which is approximately seven times higher than that of the pure MoS_2-based sensor (6.4%). The sensor also achieved relatively short response/recovery times and full recovery properties. Notably, the optimal sensor displayed extraordinary selectivity towards NO_2, showing negligible responses to different interfering gases. Density functional theory calculations were conducted to elucidate the underlying sensing mechanism, which was attributed to the enhanced specific surface area, the receptor function of both PbS QDs and $PbMoO_4$ nanoparticles, along with the transducer function of MoS_2 nanosheets.

Keywords: PbS quantum dots, $PbMoO_4$, MoS_2, NO_2, selective sensing, room temperature

1. Introduction

The escalating global concern over the detection of toxic and hazardous gases grows up rapidly, promoting substantial attention in advanced sensing technologies. Among various harmful gases, NO_2 is commonly produced by vehicular exhaust, the manufacturing industry, and thermal power generation. The acid rain and photochemical smog induced by NO_2 pose substantial damage to the vulnerable ecosystem [1]. Exposure to NO_2 potentially causes irreparable damage to the human, leading to respiratory disease and cardiovascular issues. Therefore, developing effective technologies for NO_2 detection holds profound significance for economic prosperity, environmental protection, and ensuring human safety [2].

Traditional resistive semiconductor gas sensors, predominantly composed of metal oxide, are subjected to the restrictions of elevated operating temperatures (typically exceeding 200 °C) and poor selectivity [3]. As a result, the sensors exhibit considerable power consumption and encounter difficulty in accurately distinguishing gas species when inferring among various gases. Motivated by this, many attempts and efforts are devoted to the reduction of operating temperature and enhancement of gas selectivity. Room-temperature gas sensors offer significant advantages over high-temperature counterparts in terms of energy efficiency, safety, portability, and long-term stability. High-temperature sensors, requiring elevated operational temperatures to facilitate gas detection, consume more energy and pose greater safety risks, particularly when detecting flammable gases. Additionally, prolonged high-temperature operation can induce grain growth in sensing materials, leading to sensor degradation

and reduced stability. In contrast, room-temperature sensors avoid these issues, offering a more energy-efficient and portable solution with greater long-term reliability. These advantages make room-temperature gas sensors highly appealing for future applications, aligning with current technological trends and sustainability goals. A variety of novel semiconductor nanostructures are constructed to replace the traditional mono-component single-metal oxide sensing material, basically including ZnO, SnO_2, Co_2O_3 and In_2O_3, etc [4-7]. Construction of heterostructures capitalizing on the diverse excellent properties of individual components is considered as an effective method to address these issues [8, 9].

Quantum dots (QDs) emerging as a new type of semiconductor, are widely regarded as having the potential to break through the limitations of traditional sensing materials, owing to their small dimensions and exceptional electric properties. QDs have been fabricated into gas sensors and achieve high sensor response along with good selectivity [10]. Especially, PbS QDs stand out among various quantum dots, owing to low-cost fabrication compatibility, narrow band gap (0.95 eV), and large specific area [11]. Furthermore, the zero-dimensional PbS QDs are proven to be attractive additives for hybrid materials in NO_2 sensor applications [12]. Bimetal oxide including $ZnSnO_3$, $LaFeO_3$, and $CuWO_4$ etc, provides several advantages over single metal oxide in gas sensor applications [13-16]. The presence of diverse metal cations offers additional active sites for gas adsorption, consequently leading to an enhanced sensor response. Besides, the complex structure of bimetal oxide allows for the modulation of the interaction between different metal elements [17, 18], enhancing the accuracy identification of gases. The n-type bimetal oxide semiconductor material of $PbMoO_4$ is utilized to decorate MoO_3 for sensing enhancement, indicating significant potential for further development in gas

sensors [19]. MoS_2, derived from the natural mineral molybdenite, is abundant in nature and has been identified as a promising candidate for gas sensing applications due to its unique physical and chemical properties. By processing molybdenite into a functional gas sensing material, its value is significantly enhanced, providing a sustainable and high-value use for this naturally occurring mineral [20]. Besides, MoS_2 is also demonstrated as a promising substrate in the fabrication of hybrid material, due to the high carrier mobility facilitating the collection of the generated electrons in sensing reaction and offering numerous edge sites for the nucleation of decoration phase material [21].

Considering the individual advantages of PbS QDs, $PbMoO_4$ and MoS_2, designing heterostructures that integrate these components offers a feasible way to maximize their collective strengths. Motivated by this, PbS QDs-$PbMoO_4$-MoS_2 ternary nanocomposites were fabricated for highly selective NO_2 sensing at room temperature through a straightforward in-situ synthesis route. The optimal sensor based on PbS QDs-$PbMoO_4$-MoS_2 ternary nanocomposites exhibited a high response to NO_2 at 25°C, as well as extraordinary selectivity. The enhanced sensing mechanism was systematically discussed based on the microstructure characterization and density functional theory (DFT) calculation. It was attributed to the synergistic effect of the improved specific surface area, receptor function of PbS QDs and $PbMoO_4$ nanoparticles, and transducer function of MoS_2. The ternary nanocomposites exhibited broad prospects in highly selective sensing NO_2 at room temperature.

2. Experimental

2.1 Synthesis of PbS QDs-$PbMoO_4$-MoS_2 ternary nanocomposites

The detailed synthetic methods for MoS_2 materials were improved based on our previous work, as given in the supplementary material [22]. Fig. 1 illustrates the schematic diagram of the synthesis

process of PbS QDs-$PbMoO_4$-MoS_2 ternary nanocomposites. First, MoS_2 powder (0.1 g) was evenly dispersed in 10 mL absolute ethanol by ultrasonic treatment for 30 min. Consequently, predetermined concentrations (8.32, 10.4, 12.48, 14.56 and 16.64 mM) of $PbNO_3$ and NaS_2 were dissolved into 20 mL aqueous solution, respectively. Next, $PbNO_3$ aqueous solution was transferred into MoS_2 suspension with vigorously stirring for 20 min. In the process, excessive Pb^{2+} was absorbed on the surface of MoS_2, and $PbMoO_4$ nanoparticles were subsequently generated, forming the binary nanocomposites of $PbMoO_4$-MoS_2. After that, NaS_2 aqueous solution was dropwise added into the above suspension, which was under continuous stirring by employing a burette for 20 min. Then, the achieved precipitates were collected and rinsed with absolute ethanol and water through centrifugation to remove the extra ions. Finally, the above products were subjected to a vacuum oven at 60 °C to obtain PbS QDs-$PbMoO_4$-MoS_2 ternary nanocomposites, which were named as PM-26.6%, PM-33.25%, PM-39.9%, PM-46.55%, and PM-53.2% referring to the Pb/Mo molar ratios.

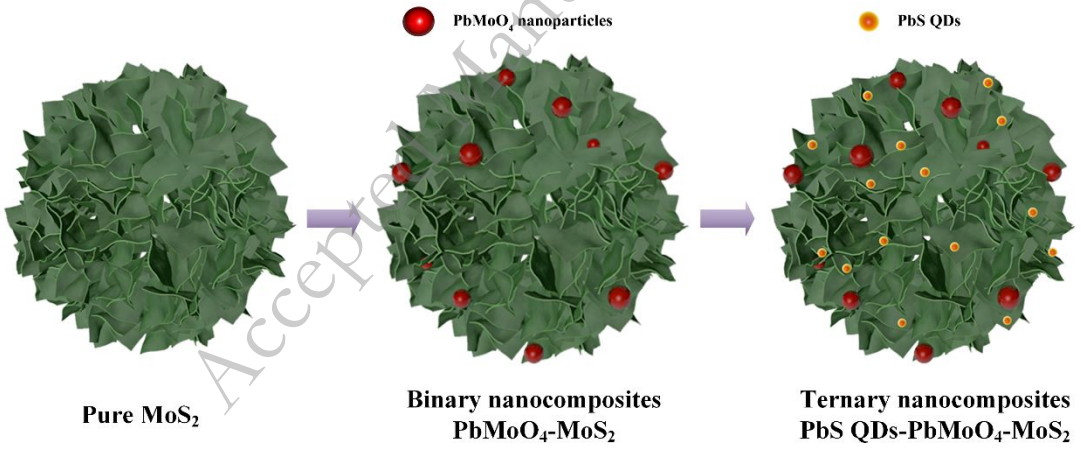

Fig. 1. Schematic illustration of the synthesis process of PbS QDs-$PbMoO_4$-MoS_2 ternary nanocomposites

2.2 Sensor fabrication and sensing measurement

Typically, the ethanol suspension of PbS QDs-$PbMoO_4$-MoS_2 ternary nanocomposites was distributed on an Au interdigital electrode (fringe spacing of 150 μm), as described in our previous work [23]. The as-fabricated sensors were dried naturally without heating and then aged at 50 °C to improve the stability. The CGS-MT (Beijing, Sino Aggtech) was utilized to measure sensing performance of the sensor device at an operating temperature of 25 °C. Furthermore, the relative humidity was measured at approximately 25 °C with values ranging between 10% and 45% RH. The sensor response was defined as $S = |R_a-R_g|/R_a \times 100\%$, where R_a and R_g represent the resistance of the sensors in the atmosphere of fresh air and target gases, respectively. The response and recovery times were defined as the duration for sensor resistance change of $90\%|R_a-R_g|$.

3. Results and Discussion

3.1 Material characterizations

Fig. S1 illustrates the surface morphologies of pure MoS_2 and PM-46.55% sample under different fields of view. Visually, pure MoS_2 exhibits a hierarchical flowerlike shape assembled from a majority of ultrathin nanosheets with an average thickness of ~7 nm. Besides, quite a few nanoparticles with average size of approximately 10 nm are uniformly in-situ dispersed on the surface of MoS_2 nanosheets, which is ascribed to the modification of PbS QDs and $PbMoO_4$ nanoparticles. Fig. 2(a-d) shows different fields of view for the TEM images of PM-46.55% sample. It is found that PbS QDs and $PbMoO_4$ nanoparticles predominantly localize at the edge side of MoS_2 nanosheets, which is consistent with our previous report [22]. The HRTEM image reveals that PbS QDs are basically less than 10 nm, whereas the size of $PbMoO_4$ nanoparticles is in the range of 10-20 nm, as

shown in Fig. 2(e). Furthermore, several PbS QDs contact with $PbMoO_4$ nanoparticles to form heterojunction without excessive agglomeration, enhancing the transport of charge carriers. Meanwhile, the interplanar lattice spacings of 0.301 nm and 0.251 nm correspond to the (200) and (202) planes of PbS and $PbMoO_4$, respectively. Fig. 2(f) presents the SAED pattern of PM-46.55% sample, indicating a polycrystalline structure. The diffraction rings refer to the planes of PbS, $PbMoO_4$, and MoS_2, proving the successful construction of ternary heterostructure. The selected area of the sample for applying EDS mapping coupled with TEM is illustrated in Fig. 2(g-k). As a result, the distribution of Mo, S, Pb, and O signals are uniform, indicating that PbS QDs and $PbMoO_4$ nanoparticles are attached on the nanosheets evenly.

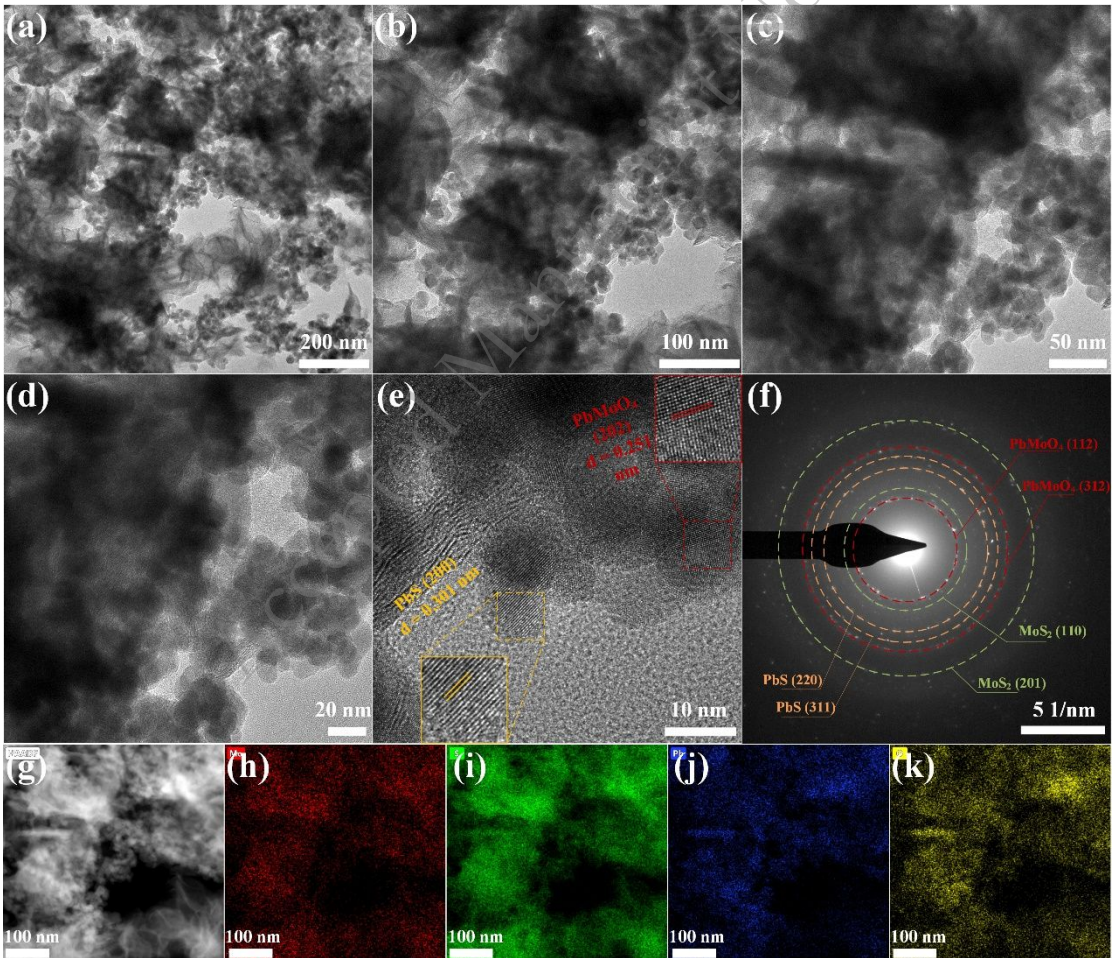

Fig. 2. (a-d) Low-magnification TEM images of PM-46.55% nanocomposites. (e) High-resolution TEM (HRTEM) image of PM-46.55% nanocomposites. The inset figures display the clear lattice

fringes. (f) Selected area electron diffraction (SAED) patterns of PM-46.55% nanocomposites. (g) HAADF image of a selected area of PM-46.55% nanocomposites, and (h-i) corresponding elemental mappings of Mo, S, Pb, and O elements distribution within the nanocomposites.

The formation of multi-metal oxide $PbMoO_3$ are independent of the drying process after collecting the product of centrifugation. The XRD patterns of the samples drying in the vacuum oven are illustrated in Fig. S2, in which the typical characteristic peaks referring to $PbMoO_3$ are clearly observed. The attachment of Pb^{2+} on the surface of MoS_2 possibly in-situ transforms MoO_3 into $PbMoO_4$ nanoparticles with the help of water, as shown in the equation (1) [24]. With the addition of Pb^{2+} in the aqueous solution, MoO_3 oxidation layer on MoS_2 nanosheets is etched into small nanoparticles. Besides, MoS_2 is reported to gradually dissolve in water with the presence of oxygen and subsequently generate MoO_4^{2-}, as described in the equation (2). Moreover, the defects on MoS_2 nanosheets with high reactivity are easy to absorb Pb^{2+} and then interact with MoO_4^{2-} to form $PbMoO_4$ nanoparticles, which may be another possible reaction pathway [25]. EPR was conducted on the MoS_2 and PbS quantum dots-$PbMoO_4$-MoS_2 ternary nanocomposite to investigate the presence of vacancies, as shown in Fig. S3. The results revealed a weak characteristic peak at a g-factor of 1.999 for both samples, indicating the presence of a small number of sulfur vacancies. Moreover, the peak intensity for MoS_2 was higher than that of the PbS quantum dots-$PbMoO_4$-MoS_2 ternary nanocomposites, suggesting that the introduction of PbS QDs tends to promote growth at defect sites, thereby reducing the number of vacancies.

$$MoO_3 + H_2O + Pb^{2+} \rightarrow PbMoO_4 + 2H^+ \quad (1)$$

$$MoS_2 + \frac{9}{2}O_2 + 3H_2O \rightarrow MoO_4^{2-} + 2SO_4^{2-} + 6H^+ \quad (2)$$

XRD patterns of pure MoS2, PbS and PbS QDs-$PbMoO_4$-MoS_2 ternary nanocomposites with different Pb/Mo molar ratios are shown in Fig. 3(a). For pure MoS_2, the peaks at approximately 9°, 33°, and 57° can be well assigned to the (002), (100), and (110) planes of hexagonal MoS_2 (ICDD card No. 75-1539). The identified (111), (200), and (220) diffraction peaks of PbS at approximately 26°, 30°, and 43° are observed, which refers to the cubic PbS (ICDD card No. 05-0592). Obviously, the corresponding peaks are also observed in all PbS QDs-$PbMoO_4$-MoS_2 ternary nanocomposites. Besides, the diffraction peaks at approximately 18° and 27° can be well indexed to the (101) and (112) planes, which are in accordance with tetragonal $PbMoO_4$ (ICDD card No. 44-1486). The presence of the above characteristic peaks indicates the formation of ternary heterostructures. With increasing Pb components in the nanocomposites, the intensity of diffraction peaks of $PbMoO_4$ decreases, especially for the (112) peak. Meanwhile, the peaks belonging to PbS clearly sharpen, which is ascribed to the additional formation of PbS QDs. The Raman spectra of pure MoS_2 and PbS QDs-$PbMoO_4$-MoS_2 ternary nanocomposites are presented in Fig. 3(b). The characteristic peaks at approximately 376 cm^{-1} and 406 cm^{-1} are corresponded to E_{2g}^1 and A_{1g} modes of MoS_2 [26]. These two peaks are also observed in the spectra of ternary nanocomposites. However, two peaks at around 317 cm^{-1} and 868 cm^{-1} appear apparently, which are attributed to the $v_2(B_g, A_g)$ and $v_1(A_g)$ modes of $PbMoO_4$. The two peaks are attributed to the symmetric and antisymmetric stretching of the MoO_4^{2-} group and the characteristic symmetric stretching of molybdates [27, 28].

Fig. 3(c) shows the BET surface area of pure MoS_2 and PM-46.55% sample, which are calculated to be 22.08 m^2/g and 33.50 m^2/g, respectively. Apparently, the BET surface area of PbS QDs-$PbMoO_4$-MoS_2 ternary nanocomposites is substantially enhanced after the attachment of PbS QDs

and $PbMoO_4$ nanoparticles. The defects and vacancies on the edge side of MoS_2 nanosheets offer numerous nucleation sites for the decoration phases of PbS QDs and $PbMoO_4$ nanoparticles, which shows a large specific surface area. The improved large specific surface area exposes additional active centers for the interaction of electrons with gas reactants, which is conducive to the gas sensing properties.

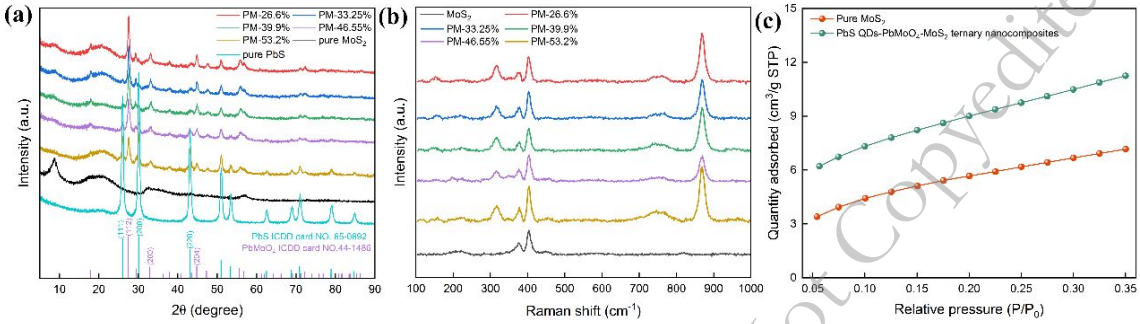

Fig. 3. (a) XRD patterns of pure MoS_2, PbS and PbS QDs-$PbMoO_4$-MoS_2 ternary nanocomposites with different Pb/Mo molar ratios. (b) Raman spectra of pure MoS_2 and PbS QDs-$PbMoO_4$-MoS_2 ternary nanocomposites. (c) BET surface area of pure MoS_2 and PM-46.55% nanocomposites.

Fig. 4 illustrates the XPS spectra of the PM-46.55% sample to investigate the elemental composition and chemical states. As illustrated in the Mo 3d spectra (Fig. 4(a)), the doublet characteristic peaks at 232.1 eV and 228.8 eV, corresponding to Mo $3d_{3/2}$ and Mo $3d_{5/2}$, respectively, indicate the Mo predominantly exist in the +4 state [29]. Besides, the peak at a higher binding energy of 235.8 eV is attributed to the presence of Mo^{6+}, which is ascribed to Mo^{6+} ions in $PbMoO_4$ [30]. Furthermore, a characteristic peak at a lower binding energy of 226.1 eV is observed, corresponding to S 2s peak in Fig. 4(b). The doublet characteristic peaks at binding energies of 163.1 eV and 161.6 eV are observed, indicating the presence of S^{2-}. Observation of two new peaks at 168.8 eV and 165.1 eV are corresponding to the S-O bond and edge sulfur, respectively. The phenomenon confirms the sulfur

partial oxidation and generation of vacancies and defects at S sites [31, 32]. As illustrated in Fig. 4(c), the Pb 4f spectra can be perfectly fit into four peaks at 143.9 eV, 142.7 eV, 139.1 eV and 137.9 eV, respectively. These peaks correspond to Pb $4f_{5/2}$ and Pb $4f_{7/2}$, indicating the presence of Pb^{2+} ions in the ternary nanocomposites [33]. For the O 1s in Fig. 4(d), the characteristic peaks assigned to lattice oxygen, adsorbed oxygen, and hydroxyl are observed at 530.8 eV, 531.8 eV, and 533.6 eV, respectively. The results confirm the presence of $PbMoO_4$ in the ternary nanocomposites and the generation of vacancies and defects, which facilitates the gas sensing adsorption [34].

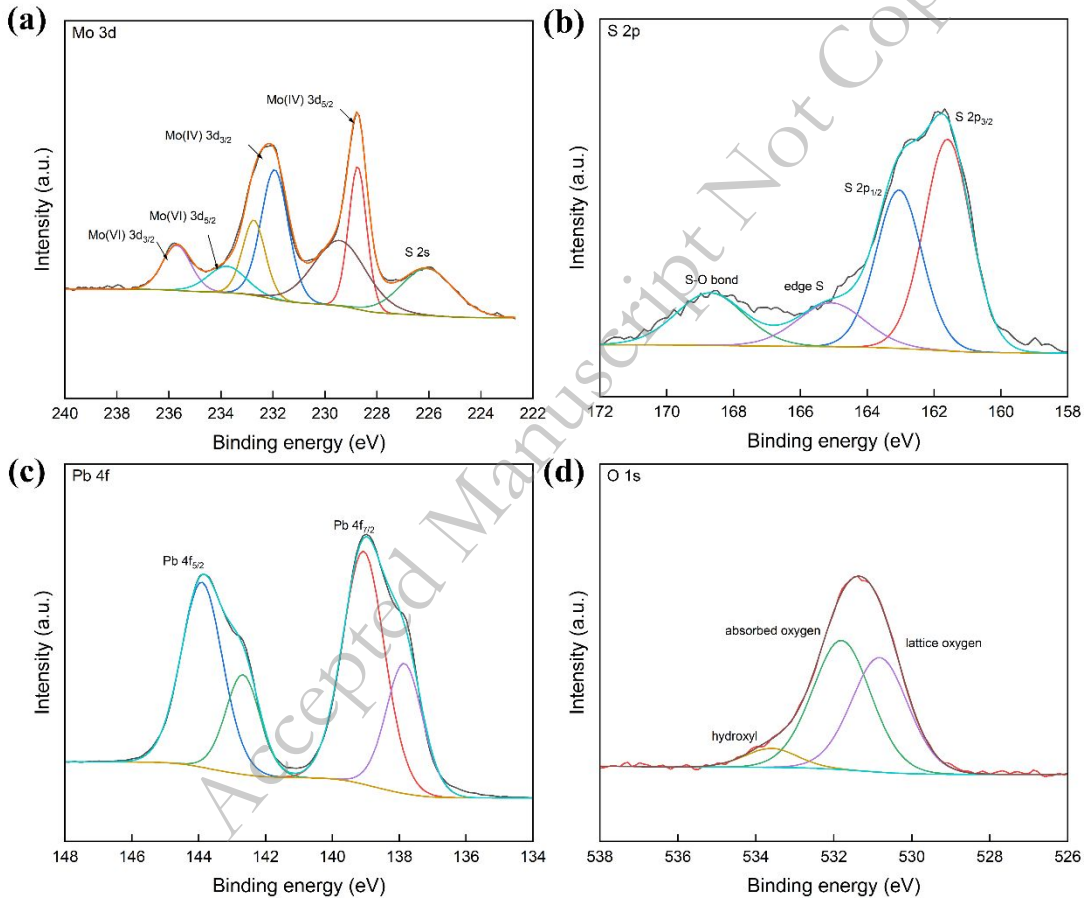

Fig. 4. (a) XPS spectra of (a) Mo 3d, (b) S 2p, (c) Pb 4f, and (d) O 1s of PM-46.55% nanocomposites.

In Fig. S4(a), the XPS survey spectrum for pure MoS_2 identifies the presence of Mo, S, and O signals. Moreover, Mo, S, Pb, and O elements are observed in the XPS survey spectrum for PM-46.55%

ternary nanocomposites. To note, the intensity of the peaks for O 1s for pure MoS_2 is lower than that for ternary nanocomposites, which is ascribed to the formation of $PbMoO_4$ nanoparticles. As given in Fig. S4(b), the doublet high-intensity characteristic peaks in Mo 3d spectra for pure MoS_2 demonstrate the presence of Mo^{4+}. A relatively low-intensity peak located at 236.1 eV presents the +6 state, demonstrating the transition from Mo^{4+} to Mo^{6+} during MoS_2 slightly oxidation process [35]. The spectra of S 2p for pure MoS_2 in Fig. S4(c) is similar as that of ternary nanocomposites, whereas the intensity peak assigning to S-O bond is relatively low, indicating the slight oxidation of sulfur for pure MoS_2. Obviously, the O 1s spectrum is mainly ascribed to the adsorbed oxygen and no typical characteristic peak for lattice oxygen is observed, which is may be due to the relatively slight oxidation (Fig. S4(d)).

Considering the crucial role of PbS QDs in the sensing reaction, PbS-MoS_2 model is chosen to represent the complex PbS QDs-$PbMoO_4$-MoS_2 ternary nanocomposites in DFT calculation [36, 37]. Fig. 5(a-h) displays the optimized structure and Mulliken population of MoS_2, NO_2-MoS_2, PbS-MoS_2, NO_2-PbS-MoS_2, respectively, from both top view and side view. As shown in Fig. 5(a, b), the charges of Mo and S atoms for pure MoS_2 are 0.07 e and –0.03 e, respectively. When NO_2 approaches to the pure MoS_2, the charges of Mo and S atoms closing to NO_2 molecule change to be 0.06 e and –0.02 e, respectively. However, the charges of Mo and S atoms located relatively far from NO_2 molecule show no difference (Fig. 5(c, d)). As shown in Fig. 5(e, f), after the contact between PbS and MoS_2, the charges of Mo and S atoms decrease, indicating the electrons transfer from PbS to MoS_2 and the successful construction of heterojunction [38]. When NO_2 molecule is absorbed on PbS, the charges of adsorption Pb site change to be 0.71 e from 0.61 e, as illustrated in Fig. 5(g, h). Additionally, the

charges of S atoms closest to the adsorption Pb site change from –0.61 e to –0.57 e. Compared with NO_2-MoS_2 system, the negative charge accumulates more on NO_2 molecule in the NO_2-PbS-MoS_2 system, indicating NO_2 captures more free electrons from PbS-MoS_2 than pure MoS_2. Furthermore, in the NO_2-PbS-MoS_2 system, the charge distribution on MoS_2 surface also slightly changes, confirming that the charges generated in the adsorption process transfer from PbS to MoS_2 through the heterojunction channel. After that, the free electrons generated in the sensing process are transferred to the electrodes through the conductive pathway of MoS_2 for collection.

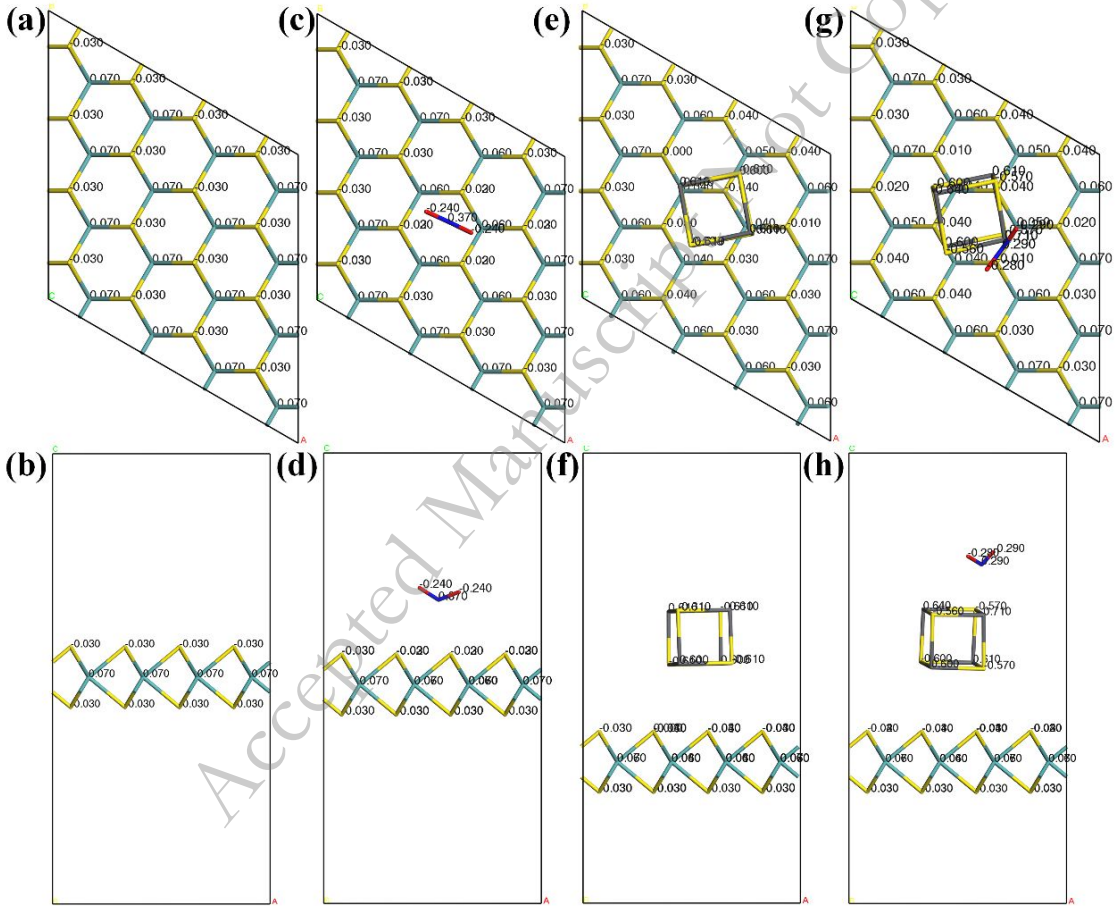

Fig. 5. (a-d) Top view and (e-h) side view of the optimized structure and Mulliken population of MoS_2, NO_2-MoS_2, PbS-MoS_2, NO_2-PbS-MoS_2 system.

The adsorption parameters of NO_2-MoS_2 and NO_2-PbS-MoS_2 models are given in Table. 1. The adsorption distance of NO_2-MoS_2 system is longer than that of NO_2-PbS-MoS_2 system, indicating the weak adsorption of NO_2 on MoS_2 surface. Besides, the small charge transfer of adsorption energy for NO_2-MoS_2 system also confirms the intensive NO_2 adsorption on MoS_2. Though the negative value of adsorption energy proves the adsorption process proceeds spontaneously, the sensing reaction is still weak due to the low absolute value of adsorption energy. The adsorption site for NO_2-MoS_2 system possibly occurs at the S sites whereas the adsorption site for NO_2-PbS-MoS_2 is Pb site from PbS. The shortened bond distance, along with the increased absolute values of charge transfer and adsorption energy, demonstrates a strong interaction between the NO_2 molecule and PbS-MoS_2. This confirms that the addition of PbS QDs significantly enhances the sensing performance of pure MoS_2.

Table 1. Adsorption parameters of NO_2 on MoS_2 and PbS-MoS_2

Adsorption system	Bond	Distance (Å)	Charge transfer (e)	Adsorption energy (eV)
NO_2-MoS_2	N-S	3.153	–0.11	–0.07947
NO_2-PbS-MoS_2	N-Pb	2.625	–0.28	–0.35597

To investigate the effect of heterojunction formation and NO_2 adsorption on electronic properties, the TDOS curves are analyzed in Fig. 6. Fig. 6(a) displays the TDOS curves of MoS_2 and PbS-MoS_2, showing that the TDOS of PbS-MoS_2 shifts to left significantly. Furthermore, two new peaks at around –6.8 eV and –10.6 eV appear, which is possibly due to the overlapping of the density states of PbS and MoS_2. The results prove that a large amounts of charge transfer and heterojunction formed between PbS and MoS_2. As illustrated in Fig. 6(b), the TDOS curve of NO_2-MoS_2 slightly shifts to right, indicating that the adsorption of NO_2 molecule influences the electron orbitals of MoS_2. Meanwhile, some new peaks occur at approximately –7.3 eV and –10.2 eV, which are ascribed to the NO_2 molecule.

However, the difference between the TDOS curves of MoS_2 and NO_2-MoS_2 is small, indicating the weak adsorption of NO_2 on MoS_2. Compared with the system of NO_2-MoS_2, the TDOS curve of NO_2-PbS-MoS_2 shifts to left notably, indicating a strong interaction between NO_2 and MoS_2, as given in Fig. 6(c). The substantial change proves that the decoration of PbS predominantly enhances the sensitivity to NO_2.

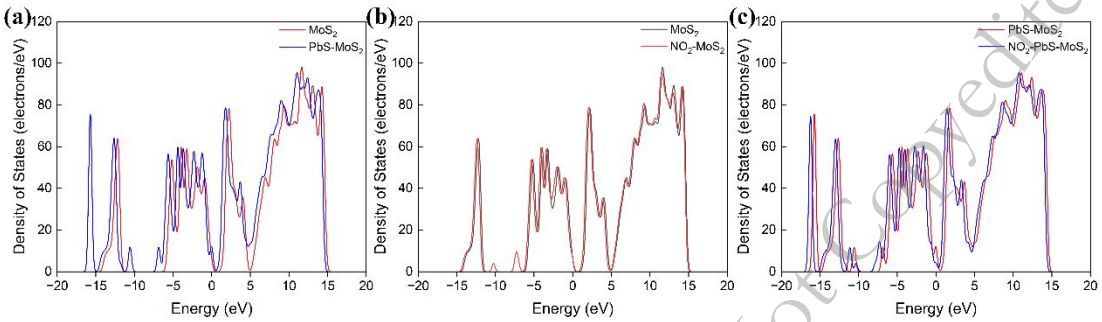

Fig. 6. (a) TDOS curves of MoS_2 and PbS-MoS_2. (b) TDOS curves of MoS_2 and NO_2-MoS_2 system. (c) TDOS curves of PbS-MoS_2 and NO_2-PbS-MoS_2 system.

The PDOS curves of MoS_2, NO_2-MoS_2, and PbS-MoS_2 are given in the supplementary material (Fig. S5-Fig. S7). It is because that the total density of states is greatly affected by the electron in the outer orbit of the atom, the partial density of states in some outer orbits is primarily investigated in the PDOS curve of NO_2-PbS-MoS_2 system, as shown in Fig. 7(a). The density of states predominantly occurs in the range of –8 eV to 5 eV, and the overlapping parts suggest the orbitals hybridization in the adsorption process. Notably, the Pb 5p orbital hybridizes with N 2p and O 2p orbitals in the range of 2 eV to 5 eV, indicating that strong interaction and adsorption occur between the decoration phase of PbS and NO_2 molecule. Fig. 7(b-f) displays the PDOS curves of Mo, S, Pb, N and O elements, respectively. The electron states near the Fermi level are primarily contributed by Mo 4d, S 3p, Pb 5p, N 2p and O 2p for each element. The above orbitals are more likely to hybridize with other orbitals and then form bonds, finally affecting the sensing reaction. In addition, the interaction and charge transport in

PbS-MoS_2 and NO_2-PbS-MoS_2 systems are also evaluated by electron density difference (EDD) analysis, as displayed in Fig. S8.

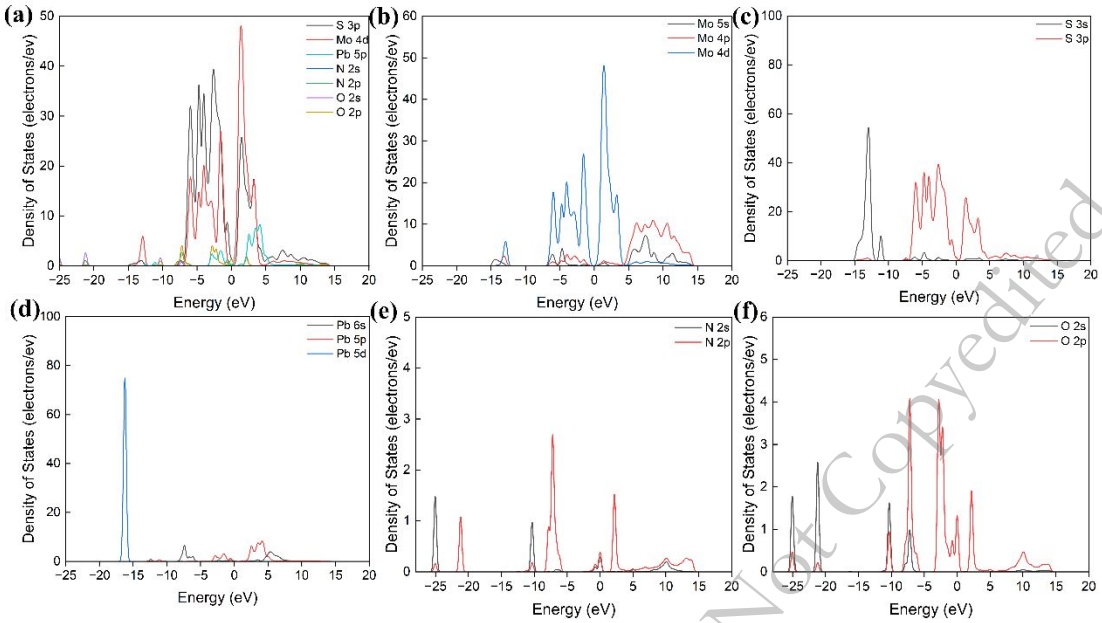

Fig. 7. (a) PDOS curves of NO_2-PbS-MoS_2 system. (b-f) PDOS curves of Mo, S, Pb, N, and O elements in NO_2-PbS-MoS_2 system.

3.2 NO_2 sensing properties

Fig. S9 illustrates the dynamic response-recovery curves of pure MoS_2 based sensor to gradient concentrations of NO_2 ranging from 1-20 ppm at 25 °C. It is found that this sensor exhibits a low response of 19.9% even to a high concentration of 20 ppm. To systematically investigate the gas sensing properties of the obtained ternary nanocomposites with different Pb/Mo molar ratios, Fig. 8(a) evaluates the dynamic sensing response of the sensors to 1 ppm NO_2 at room temperature of 25 °C and relative humidity of 20%RH. It can be seen that the responses of PbS QDs-$PbMoO_4$-MoS_2 ternary nanocomposites based sensors far surpass the response value of pure MoS_2. Among the sensors constructed from ternary nanocomposites with different Pb/Mo molar ratios, the PM-46.55% sensor exhibits the highest sensor response of 44.5%, which is approximately 7-fold as the response value of

6.5% for pure MoS_2 to 1 ppm NO_2. The results demonstrate that the attachment of PbS QDs and $PbMoO_4$ nanocomposites significantly improves the sensing performance. The inset figure illustrates the I-V curves of the sensors based on PbS QDs-$PbMoO_4$-MoS_2 ternary nanocomposites. The linear relationship between current and voltage signifies the ohmic contact, ensuring a stable and predictable electrical response to detected gas.

The dynamic response curves of the sensors based on PbS QDs-$PbMoO_4$-MoS_2 ternary nanocomposites to various concentrations of NO_2 were examined, and the corresponding results are given in Fig. 8(b). The response values of the optimal sensor based on PM-46.55% sample are 47.4%, 57.4%, 62.5%, 66.1%, 78.5%, and 73.0% to 1, 2, 3, 4, 5, and 10 ppm NO_2. In addition, when the gradient concentrations of NO_2 are below 5 ppm, the response value increases linearly, as illustrated in Fig. 8(c). Furthermore, the relationship between sensor response and NO_2 concentration for this optimal sensor can be represented as $S = 45.11 + 5.9\ C$, which facilitates the rapid detecting and accurate quantifying of the NO_2 in actual applications (Fig. 8(d)). However, only polynomial equations can be used for fitting the relationship between response value and NO_2 concentration once NO_2 concentrations above 10 ppm. The phenomenon is possibly ascribed to the saturation adsorption of NO_2 molecules onto the surface of ternary nanocomposites, thereby preventing variations in sensor resistance.

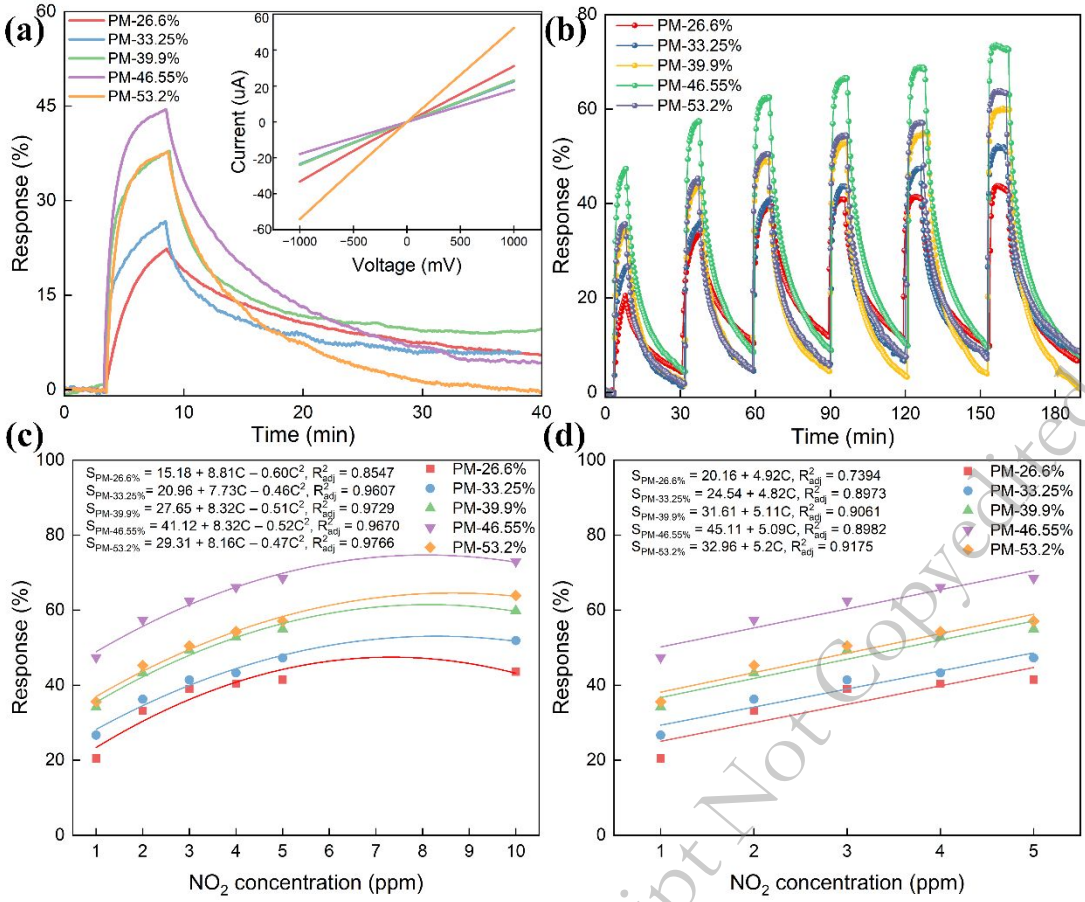

Fig. 8. (a) Dynamic sensing response of the sensors based on PbS QDs-$PbMoO_4$-MoS_2 ternary nanocomposites to 1 ppm NO_2 at room temperature of 25 °C. The inset figure shows the I-V curves of the sensors. (b) Dynamic response curves of the sensors based on PbS QDs-$PbMoO_4$-MoS_2 ternary nanocomposites to various NO_2 concentrations in the range of 1~10 ppm. (c) Relationship between sensor response and NO_2 concentration. (d) Linear relationship between sensor response and NO_2 concentration in the range of 1~5 ppm.

Repeatability and long-term stability referring to the properties of the sensors maintain accuracy over an extend period, significantly determining the practicality of the sensors. To comprehensively investigate the repeatability of the sensors based on PbS QDs-$PbMoO_4$-MoS_2 ternary nanocomposites, which are subjected to 4 cycles of 1 ppm NO_2, as illustrated in Fig. 9(a). All the sensors based on ternary nanocomposites exhibit consistent response and recovery properties, indicating an exceptional

repeatability to NO_2. The long-term stability of the optimal PM-46.55% sensor is evaluated by continuously exposing to 1 ppm NO_2 in 30 days, as given in Fig. 9(b). Apparently, the sensor exhibits almost no decreased response in a period of 30 days, confirming an excellent long-term stability. Besides, despite the variation of relative humidity in a relatively wide range of 10%-40%RH, the sensor response shows a slight decrease and maintains an extraordinary response higher than 42%. The results demonstrate that the sensor also has good moisture resistance to some extent. Fig. 9(c) shows the resistance changes of the PM-46.55% sensor to 1 ppm NO_2, demonstrating suitable response/recovery times (128 /1510 s) and full recovery properties. Obviously, the sensor resistance decreases dramatically after contacting with the oxidating gas of NO_2, confirming a p-type semiconducting behavior of the sensor. Selectivity is another crucial parameter for gas sensors in ensuring accurate detection. Thus, the sensor responses to 1 ppm NO_2 and other six types of interfering gases including 100 ppm methanol, 100 ppm ethanol, 100 ppm acetone, 100 ppm sulfur dioxide, 100 ppm propanol, and 100 ppm ammonia are given in Fig. 9(d). The sensor shows the highest response to NO_2, which is tens to hundreds of times higher compared with the interfering gases, beneficial to distinguishing target gases in complicated environments. The pure MoS_2 sensor has poor selectivity across a range of gases, as shown in Fig. S10. As shown in Fig. S11, the water contact angle of pure MoS_2 and PbS quantum dots-$PbMoO_4$-MoS_2 ternary nanocomposites are measured to be 62.29° and 66.74°, respectively, to investigate the humidity tolerance of both sensors. A comparison of the sensor performance between this work and reported literatures is summarized in Table S1 and the results show that PbS quantum dots-$PbMoO_4$-MoS_2 ternary nanocomposites-based gas sensors promising candidates for detecting NO_2 gas in practical applications.

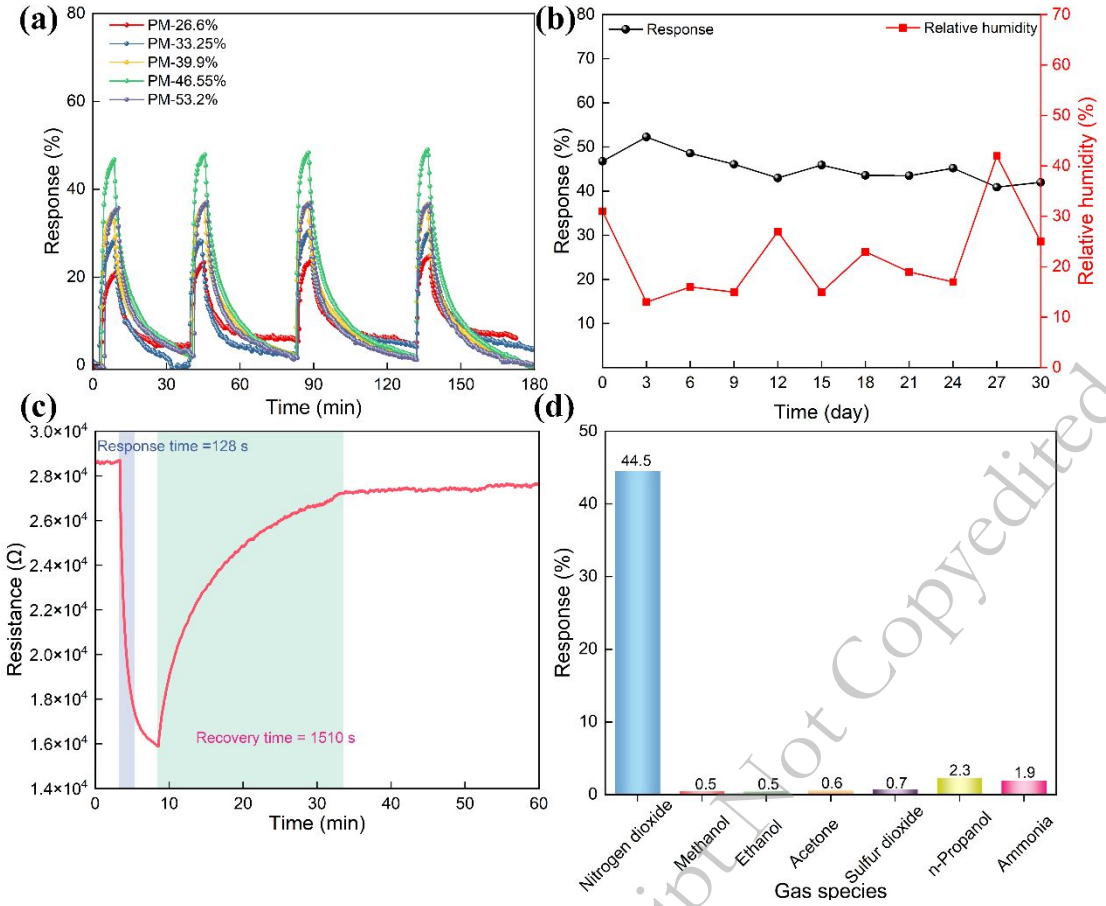

Fig. 9. (a) Repeatability of the PM-46.55% sensor to 1 ppm NO_2 for four successive cycles. (b) Long-term stability of the PM-46.55% sensor to 1 ppm NO_2 in 30 days. (c) Response and recovery times of the PM-46.55% sensor to 1 ppm NO_2. (d) Selectivity of the PM-46.55% sensor to 1 ppm NO_2 and six types of interfering gases with suitable concentrations.

3.3. Gas sensing mechanism

The sensing performance toward NO_2 for the sensor based on PbS QDs-$PbMoO_4$-MoS_2 ternary nanocomposites is superior to the sensor based on pure MoS_2 at 25°C. The enhanced sensing performance is attributed to the synergistic effects of the substantially improved specific surface area, the exceptionally high reactivity of PbS QDs and $PbMoO_4$ nanoparticles as receptors [39, 40], along with the transducer function arising from MoS_2 with efficient carrier mobility [41, 42].

As discussed in the BET results, the specific surface area of PbS QDs-$PbMoO_4$-MoS_2 ternary nanocomposites is significantly enhanced after the decoration of 0D PbS QDs and $PbMoO_4$ nanoparticles on the surface of MoS_2. The receptor function refers to the interaction between target gas molecules and the sensing material, typically driven by chemical adsorption, physisorption, or catalytic reactions, depending on the surface properties of the receptor materials. In this case, the ultrasmall size of PbS quantum dots (QDs), with their high specific surface area, plays a critical role in enhancing gas sensing performance [43]. The increased surface area provides additional active sites for gas molecule adsorption. PbS QDs with a majority of dangling bonds are highly reactive to gas molecules, thereby functioning as the receptor in the ternary nanocomposites during the sensing process. The DFT calculations also demonstrate that NO_2 molecules are more readily captured by PbS in the nanocomposites than by pure MoS_2 nanosheets, which further confirms the receptor role of PbS QDs. Besides, the introduction of Pb^{2+} to the surroundings of Mo atom significantly enlarges the electron density, facilitating to activation of the chemical adsorption of gas molecules [17]. Hence, $PbMoO_4$ nanoparticles also attract some parts of gas molecules, which is crucial to catching the target gases.

When the designed ternary nanocomposites are exposed to air, the free oxygen molecules are easily absorbed on the surface of the nanocomposites and then converted into active absorbed oxygen ions (O_2^- at 25°C) by capturing electrons from the conduction band as illustrated in equation (3) [44]. As a result, the hole concentrations in the sensing material increase, causing the resistance of the sensing material reduced to some extent. When the sensor contacts with NO_2, NO_2 molecules are absorbed on the surface of the ternary sensing material. The absorbed NO_2 molecules will further capture electrons from the conduction band of the sensing material and then form NO_2^-. Additionally,

since the electronegativity of NO_2 is much higher than that of oxygen, the absorbed NO_2 molecules also react with oxygen species of O_2^-, as given in equation (4) [45, 46]. This phenomenon leads to further depletion of electrons and, conversely, a sharp increase in hole concentration, and the conductivity of the gas sensor is dramatically enhanced, leading to a drastic change in the sensor current of the ternary nanocomposites [47].

$$O_2 + e^- \rightarrow O_2^- \quad (3)$$

$$NO_2 + O_2^- + 2e^- \rightarrow NO_2^- + 2O^- \quad (4)$$

Apart from the gas chemisorption process, the charge transfer contributes equally to the sensing performance, as shown in Fig. 10. Due to the difference of PbS QDs, MoS_2 and $PbMoO_4$ in work function, the electrons transfer from PbS QDs and $PbMoO_4$ to MoS_2 until the equilibrium of Fermi level [12, 48]. In sequence, numerous heterojunctions are constructed between the decoration particles and the substrate material of MoS_2, providing charge transfer channels in the sensing process. When the sensor contacts with oxidizing gas of NO_2, NO_2 molecules are more likely to be adsorbed on the receptor of PbS QDs and $PbMoO_4$ nanoparticles, injecting a concentration of holes into sensing material [49]. The transducer function is primarily governed by the substrate material of MoS_2. Specifically, when injected holes are transported to the MoS_2 smoothly through the heterojunction channel at the interface, the holes are subsequently moved on the high-mobility transport pathways of MoS_2 to the electrodes for collection [33]. The change in conductivity is then detected and quantified, enabling precise measurement of gas concentration. All of these enable the PbS QDs-$PbMoO_4$-MoS_2 ternary nanocomposite nanohybrids to exhibit excellent NO_2 sensing performance.

The strong selectivity of the PbS quantum dots-$PbMoO_4$-MoS_2 ternary nanocomposite sensor toward NO_2 can be attributed to two primary factors. First, NO_2 possesses a high electron affinity, enabling it to efficiently withdraw electrons from MoS_2, which induces significant changes in the conductivity of the sensor. Second, the integration of PbS QDs enhances the surface reactivity and adsorption capacity of MoS_2 by introducing additional active sites that are particularly favorable for NO_2 adsorption.

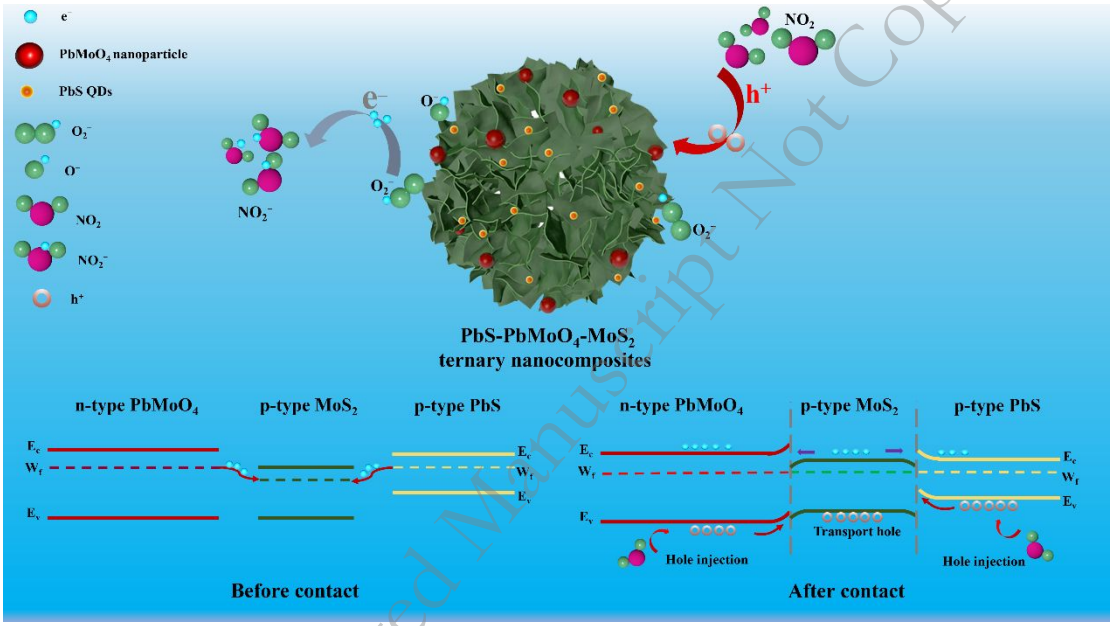

Fig. 10. Sensing mechanism of NO_2 absorbed on PbS QDs-$PbMoO_4$-MoS_2 ternary nanocomposites and schematic illustrations of the band diagram of PbS QDs-$PbMoO_4$-MoS_2 ternary nanocomposites before and after contact of the three individual phases.

4. Conclusions

PbS QDs-$PbMoO_4$-MoS_2 ternary nanocomposites were successfully synthesized through a facile in-situ synthesis process. The morphology and composition of the obtained nanocomposites were systematically investigated, showing that PbS QDs, with sizes below 10 nm, and $PbMoO_4$

nanoparticles, approximately 10-20 nm in size, were uniformly distributed on MoS_2 nanosheets. Impressively, the as-fabricated sensor exhibited an excellent response of 44.5% to 1 ppm NO_2 at 25°C, which is approximately seven times higher than that of the pure MoS_2-based sensor. Notably, the sensor also displayed remarkable selectivity toward NO_2 with negligible responses to various interfering gases. Density functional theory was employed for in-depth mechanism investigation, revealing the adsorption behavior of NO_2 on sensing material. The possible sensing mechanism was attributed to the synergistic effects of enhanced specific surface area, receptor function of zero-dimensional decoration particles, and transducer function of MoS_2 nanosheet $substrate_2$. This work highlights the potential of PbS QDs-$PbMoO_4$-MoS_2 ternary nanocomposites in highly selective NO_2 sensing at room temperature, providing a feasible way to fabricate novel high-performance sensors.

Acknowledgments

The project was supported by the National Natural Science Foundation of China (52274255), Fundamental Research Funds for the Central Universities (N2401003, N2301003, N2201008, N2201004, N2301025), Liaoning Revitalization Talents Program (XLYC2202028), Postdoctoral Foundation of Northeastern University, Young Elite Scientists Sponsorship Program by CAST (2022QNRC001), and China Postdoctoral Science Foundation (2022M720025). Special thanks are due to the instrument and data analysis from Analytica and Test Center, Northeastern University.

References

[1] D. Han, X.R Liu, D.H Li, J. Shi, Y. Wang, Y.X. Wang, H.T. Wang, and S.B. Sang., NO_2 gas sensor with high selectivity and fast response based on Pt-loaded nano-porous GaN, *Int. J. Miner. Metall. Mater.*, (2024). https://doi.org/10.1007/s12613-024-2959-8

[2] A. Azizi, M. Dogan, H. Long, J.D. Cain, K. Lee, R. Eskandari, A. Varieschi, E.C. Glazer, M.L. Cohen, and A. Zettl, High-performance atomically-thin room-temperature NO_2 sensor, *Nano Lett.*, 20(2020), p. 6120.

[3] B.X. Yang, N.V. Myung, and T.T. Tran, 1D Metal Oxide Semiconductor Materials for Chemiresistive Gas Sensors: A Review, *Adv. Electron. Mater.*, 7(2021), art. No. 2100271.

[4] Q.T. Li, W. Zeng, and Y.Q. Li, Metal oxide gas sensors for detecting NO_2 in industrial exhaust gas: Recent developments, *Sens. Actuators B Chem.*, 359(2022), art. No. 131579.

[5] G.D. Li, Y.B. Shen, S.K. Zhao, A. Li, C. Han, Q. Qiang, D.Z. Wei, Z.Y. Yuan, and F.L. Meng, Novel sensitizer Au_xSn modify rGO-SnO_2 nanocomposites for enhancing detection of sub-ppm H_2, *Sens. Actuators B Chem.*, 373(2022), art. No. 132656.

[6] F.L. Meng, X.Z. Li, Z.Y. Yuan, Y.F. Lei, T.Y. Qi, and J. Li, Ppb-level xylene gas sensors based on Co_3O_4 nanoparticle-coated reduced graphene oxide (rGO) nanosheets operating at low temperature, *IEEE Trans. Instrum. Meas.*, 70(2021), pp. 1-10.

[7] S.K. Zhao, Y.B. Shen, P.F. Zhou, F.L. Hao, X.Y. Xu, S.L. Gao, D.Z. Wei, YX. Ao, and Y.B. Shen, Enhanced NO_2 sensing performance of ZnO nanowires functionalized with ultra-fine In_2O_3 nanoparticles, *Sens. Actuators B Chem.*, 308(2020), art. No. 127729.

[8] Y. Niu, J.W. Zeng, X.C. Liu, J.L. Li, Q. Wang, H. Li, N.F. Rooji, Y.Wang, and G.F. Zhou, A photovoltaic self-powered gas sensor based on all-dry transferred MoS_2/GaSe heterojunction for ppb-level NO_2 sensing at room temperature, *Adv. Sci.*, 8(2021), art. No. 2100472.

[9] Y.L. Li, X.Y. Yu, Y.J. Zhou, Y. Lin, and Y. Wu, Nanostructured ZnO/$BiVO_4$ Ⅰ-scheme heterojunctions for piezocatalytic degradation of organic dyes via harvesting ultrasonic vibration energy, *Int. J. Miner. Metall. Mater.*, (2024). https://doi.org/10.1007/s12613-024-2920-x

[10] J.S. Yuan, Y. Zhang, X.Y. Zhang, J.J. Zhang, and S.G. Zhang, N-doped graphene quantum dot-decorated N-TiO_2/P-doped porous hollow g-C_3N_4 nanotube composite photocatalysts for antibiotic photodegradation and H_2 production, *Int. J. Miner. Metall. Mater.*, 31(2024), No. 1, pp. 165-178.

[11] I. Moreels, Y. Justo, B. Geyter, K. Haustraete, J.C. Martins and Z. Hens, Size-tunable, bright, and stable PbS quantum dots: a surface chemistry study, *ACS Nano*, 5(2011), pp. 2004-2012.

[12] J.Y. Liu, Z.X. Hu, Y.Z. Zhang, H.Y. Li, N.B. Gao, Z.L. Tian, L.C. Zhou, B.H. Zhang, J. Tang, J.B. Zhang, F. Yi, and H. Liu, MoS_2 nanosheets sensitized with quantum dots for room-temperature gas sensors, *Nano-Micro Lett.*, 12(2020), art. No. 59.

[13] D. Wang, X.X. Pu, X. Yu, L.P. Bao, Y. Cheng, J.C. Xu, S.C. Han, Q.X. Ma, and X.Y. Wang, Controlled preparation and gas sensitive properties of two-dimensional and cubic structure $ZnSnO_3$, *J. Colloid Interface Sci.*, 608(2022), pp. 1074-1085.

[14] S. Thirumalairajan, K. Girija, V.R. Mastelaro, and N. Ponpandian, Surface morphology-dependent room-temperature $LaFeO_3$ nanostructure thin films as selective NO_2 gas sensor prepared by radio frequency magnetron sputtering, *ACS Appl. Mater., Interfaces*, 6(2014), pp. 13917-13927.

[15] H. Naderi, S. Hajati, M. Ghaedi, K. Dashtian, and M.M. Sabzehmeidani, Sensitive, selective and rapid ammonia-sensing by gold nanoparticle-sensitized V_2O_5/$CuWO_4$ heterojunctions for exhaled breath analysis, *Appl. Surf. Sci.*, 501(2020), art. No. 144270.

[16] Y.Y. Yin, Y.B. Shen, P.F. Zhou, R. Lu, A. Li, S.K. Zhao, W.G. Liu, D.Z. Wei, and K.F. Wei, Fabrication, characterization and n-propanol sensing properties of perovskite-type $ZnSnO_3$ nanospheres based gas sensor, *Appl. Surf. Sci.*, 509(2020), art. No. 145335.

[17] R.S. Datta, J.Z. Ou, M. Mohiuddin, B.J. Carey, B.Y. Zhang, H. Khan, N. Syed, A. Zavabeti, F. Haque, T. Daeneke, and K. Kalantar-zadeh, Two dimensional $PbMoO_4$: A photocatalytic material derived from a naturally non-layered crystal, *Nano Energy*, 49(2018), pp. 237-246.

[18] W.B. Qin, Z.Y. Yuan, Y.B. Shen, R.Z. Zhang, and F.L. Meng, Phosphorus-doped porous perovskite $LaFe_{1-x}P_xO_{3-\delta}$ nanosheets with rich surface oxygen vacancies for ppb level acetone sensing at low temperature, *Chem. Eng. J.*, 431(2022), art. No. 134280.

[19] F.D. Zhang, K.W. Liu, H.L. Li, S.H. Cui, D.Z. Zhang, J.B. Zeng, and Z.F. Yan, MoO_3 nanorods decorated by $PbMoO_4$ nanoparticles for enhanced trimethylamine sensing performances at low working temperature, *ACS Appl. Mater. Interfaces*, 14(2022), pp. 24610-24619.

[20] X. Tian, X.X. Cui, Y.W. Xiao, T. Chen, X.C. Xiao, and Y.D. Wang, Pt/MoS_2/polyaniline nanocomposite as a highly effective room temperature flexible gas sensor for ammonia detection, *ACS Appl. Mater. Interfaces*, 15(2023), pp. 9604-9617.

[21] Z.Y. Qin, C. Ouyang, J. Zhang, L. Wan, S.M. Wang, C.S. Xie, and D.W. Zeng, 2D WS_2 nanosheets with TiO_2 quantum dots decoration for high-performance ammonia gas sensing at room temperature, *Sens. Actuators B Chem.*, 253(2017), pp. 1034-1042.

[22] J.Z. Bai, Y.B. Shen, S.K. Zhao, Y.S. Chen, G.D. Li, C. Han, D.Z. Wei, Z.Y. Yuan, and F.L. Meng, Flower-like MoS_2 hierarchical architectures assembled by 2D nanosheets sensitized with SnO_2 quantum dots for high-performance NH_3 sensing at room temperature, *Sens. Actuators B Chem.*, 353(2022), art. No. 131191.

[23] J.Z. Bai, S.K. Zhao, W.X. Wang, M.L. Wu, H. Xiao, W.B. Liu, Z.Y. Yuan, F.L. Meng, and Y.B. Shen, In-situ construction of SnO_2 nanolayer-SnS_2 nanosheets heterostructures for enhanced NO_2 sensing at room temperature and their DFT investigation, *J. Alloy. Compd.*, 1008 (2024) art. No. 176616.

[24] Y.Y. Wu, X.L. Cheng, X.F. Zhang, Y.M. Xu, S. Gao, H. Zhao, and L.H. Huo, High efficient and selective removal of Pb^{2+} through formation of lead molybdate on α-MoO_3 porous nanosheets array, *J. Colloid Interface Sci.*, 491(2017), pp. 80-88.

[25] D.O. Li, M.S. Gilliam, A. Debnath, X.S. Chu, A. Yousaf, A.A. Green, and Q.H. Wang, Interaction of Pb^{2+} ions in water with two-dimensional molybdenum disulfide, *J. Phys-Mater.*, 3(2020), art. No. 024007.

[26] Z.T. Lin, W.G. Liu, S.B. Tian, K. Zhu, Y. Huang, and Y. Yang, Thermal expansion coefficient of few-layer MoS_2 studied by temperature-dependent Raman spectroscopy, *Sci Rep*, 11(2021), art. No. 7037.

[27] A. Phuruangrat, B. Kuntalue, S. Artkla, S. Promnopas, W. Promnopas, S. Thongtem, and T. Thongtem, Effect of lead salts on phase, morphologies and photoluminescence of nanocrystalline $PbMoO_4$ and $PbWO_4$ synthesized by microwave radiation, *Mater. Sci.*, 34(2016), pp. 529-533.

[28] S. Delice, M. Isik, and N.M. Gasanly, Linear and nonlinear optical characteristics of $PbMoO_4$ single crystal for optoelectronic applications, *J. Mater. Sci.-Mater. Electron.*, 33(2022), pp. 22281-22290

[29] J.S. Yuan, Y.Zhang, X.Y. Zhang, L. Zhao, H.L. Shen, and S.G. Zhang, Template-free synthesis of core-shell Fe_3O_4@MoS_2@mesoporous TiO_2 magnetic photocatalyst for wastewater treatment, *Int. J. Miner. Metall. Mater.*, 30(2023), No. 1, pp. 177-191.

[30] H.Z. Yang, T.P. He, Y.H. Wu, J.H. Luo, A.H. Zhang, X.Y. Chen, Y.L. Zeng, Y.H. Wang, Y.L. Zhao, and G.J. Wang, Magnetically recyclable $PbMoO_4$/BC/Fe_3O_4 composite for tetracycline removal: fabrication, performance, and mechanism, *J. Mater. Sci.*, 57(2022), pp. 21853-21868.

[31] T.F. Jaramillo, K.P. Jørgensen, J. Bonde, J.H. Nielsen, S. Horch, and I. Chorkendorff, Identification of active edge sites for electrochemical H_2 evolution from MoS_2 nanocatalysts, *Science*, 317(2007), pp. 100-102.

[32] Y.C. Yang, J.P. Mao, D.M. Yin, T.Y. Zhang, C.L. Liu, W.X. Hao, Y. Wang, and J.Y. Hao, Synergy of S-vacancy and heterostructure in BiOCl/Bi_2S_{3-x} boosting room-temperature NO_2 sensing, *J. Hazard. Mater.*, 455(2023), art. No. 131591.

[33] X. Xin, Y. Zhang, X.X. Guan, J.X. Cao, W.L. Li, X. Long, and X. Tan, enhanced performances of PbS quantum-dots-modified MoS_2 composite for NO_2 detection at room temperature, *ACS Appl. Mater. Interfaces*, 11(2019), pp. 9438-9447.

[34] Y.J. Zhong, W.W. Li, X.L. Zhao, X. Jiang, S.Y. Lin, Z. Zhen, W.D. Chen, D. Xie, and H.W. Zhu, High-response room-temperature NO_2 sensor and ultrafast humidity sensor based on SnO_2 with rich oxygen vacancy, *ACS Appl. Mater. Interfaces*, 11(2019), pp. 13441-13449.

[35] B. Li, L. Jiang, X. Li, P. Ran, P. Zuo, A.D. Wang, L.T. Qu, Y. Zhao, Z.H. Cheng, and Y.F. Lu, Preparation of monolayer MoS_2 quantum dots using temporally shaped femtosecond laser ablation of bulk MoS_2 targets in water, *Sci. Rep.*, 7(2017), art. No. 11182.

[36] A. Mosahebfard, R. Safaiee, and M.H. Sheikhi, Density functional theory of influence of methane adsorption on the electronic properties of a PbS cluster, *Pramana-J. Phys.*, 93(2019), art. No. 9.

[37] L. Grajciar, PbS clusters embedded in sodalite zeolite cavities of different compositions: unraveling the structural evolution and optical properties using ab Initio calculations, *J. Phys. Chem. C*, 120(2016), pp.27050-27065.

[38] B.L. Li, Q. Zhou, R.C. Peng, Y.M. Liao, and W. Zeng, Adsorption of SF_6 decomposition gases (H_2S, SO_2, SOF_2 and SO_2F_2) on Sc-doped MoS_2 surface: A DFT study, *Appl. Surf. Sci.*, 549(2021), art. No. 149271.

[39] Y.T. Tang, Y.N. Zhao, and H. Liu, Room-temperature semiconductor gas sensors: Challenges and opportunities, *ACS Sens.*, 7(2022), pp. 3582-3597.

[40] L.C. Zhou, Z.X. Hu, H.Y. Li, J.Y. Liu, Y. Zeng, J.S. Wang, Y.F. Huang, L. Miao, G.Z. Zhang, Y.A. Huang, J.J. Jiang, S.L. Jiang, and H. Liu, Template-free construction of tin oxide porous hollow microspheres for room-temperature gas sensors, *ACS Appl. Mater. Interfaces*, 13(2021), pp. 25111-25120.

[41] X.W. Chen, T. Wang, J. Shi, W. Lv, Y.T. Han, M. Zeng, J.H. Yang, N.T. Hu, Y.J. Su, H. Wei, Z.H. Zhou, Z. Yang, and Y.F. Zhang, A novel artificial neuron-like gas sensor constructed from cus quantum dots/Bi_2S_3 nanosheets, *Nano-Micro Lett.*, 14(2021), art. No. 8.

[42] S. Singh, R.M. Sattigeri, S. Kumar, P.K. Jha, and S. Sharma, Superior room-temperature ammonia sensing using a hydrothermally synthesized MoS_2/SnO_2 composite, *ACS Omega*, 6(2021), pp. 11602-11613.

[43] J.Z. Bai, Y.B. Shen, W.X. Wang, M.L. Wu, H. Xiao, Q. Zhao, S.K. Zhao, Z.Y. Yuan, and F.L. Meng, Highly sensitive room-temperature ammonia sensor based on PbS quantum dots modified SnS_2 nanosheets and theoretical investigation on its sensing mechanism by DFT calculation. *Appl. Sur. Sci.*, 680(2024), art. No. 161324.

[44] Y.Y. Yin, Y.B. Shen, S.K. Zhao, A. Li, R.Lu, C. Han, B.Y. Cui, and D.Z. Wei, Enhanced detection of ppb-level NO_2 by uniform Pt-doped $ZnSnO_3$ nanocubes, *Int. J. Miner. Metall. Mater.*, 29(2022), No. 6, pp. 1295-1303.

[45] H.N. Bai, H. Guo, C. Feng, J. Wang, B. Liu, Z.L. Xie, F.Q. Guo, D.J. Chen, R. Zhang, and Y.D. Zheng, Light-activated ultrasensitive NO_2 gas sensor based on heterojunctions of CuO nanospheres/MoS_2 nanosheets at room temperature, *Sens. Actuators B Chem.*, 368(2022), art. No. 132131.

[46] Y. Zhou, Z.H. Hu, H.C. Zhao, Y.J. Wang, J. Li, and C. Zhou, Two-dimensional black phosphorus/tin oxide heterojunctions for high-performance chemiresistive H_2S sensing, *Anal. Chim. Acta*, 1245(2023), art. No. 340825.

[47] Z.P. Liang, M.Y. Wang, X.Z. Zhang, Z. Li, K.X. Du, J. Yang, S.Y. Lei, G.J. Qiao, J.Z. Ou, and G.W. Liu, A 2D-0D-2D sandwich heterostructure toward high-performance room-temperature gas sensing, *ACS Nano*, 18(2024), pp. 3669-3680.

[48] K.M. Nam, H.S. Park, H.C. Lee, B.H. Meekins, K.C. Leonard, and A.J. Bard, Compositional screening of the Pb–Bi–Mo–O System. Spontaneous formation of a composite of p-$PbMoO_4$ and n-Bi_2O_3 with improved photoelectrochemical efficiency and stability, *J. Phys. Chem. Lett.*, 4(2013), pp. 2707-2710.

[49] G.Q. Feng, S.Q. Wang, S.H. Wang, P.C. Wang, C.T. Wang, Y.X. Song, J.K. Xiao, and C.W. Song, Ultra-sensitive trace NO_2 detection based on quantum dots-sensitized few-layer MXene: A novel convincing insight into dynamic gas-sensing mechanism, *Sens. Actuators B Chem.*, 400(2024), art. No. 134852.